

Evolution of Zr-Bearing Dispersoids during Homogenization and their Effects on Hot Deformation and Recrystallization Resistance in Al-0.8%Mg-1.0%Si Alloy

A. Elasheri^{a,*}, E.M. Elgallad^a, N. Parson^b, X.-G. Chen^a

^a Department of Applied Science, University of Quebec at Chicoutimi, Saguenay (QC), Canada G7H 2B1

^b Arvida Research and Development Centre, Rio Tinto Aluminum, Saguenay (QC), Canada G7S 4K8

Abstract

The precipitation behavior of Zr-bearing dispersoids in an Al-0.8%Mg-1.0%Si alloy was investigated for different homogenization treatments (450-550 °C). The effect on the recrystallization resistance of the alloy was also studied during post-deformation annealing. With an addition of 0.2 wt.% Zr, two different Zr-bearing dispersoids were observed depending on the homogenization conditions. Homogenization at 450 °C for 2 h resulted in the precipitation of fine and dense $L1_2$ -Al₃Zr dispersoids (8-10 nm), which were found to be coherent with the matrix. In contrast, extended homogenization times, such as 12 h at 450 °C, or increasing the homogenization temperature to 500-550 °C produced elongated DO₂₂-(Al,Si)₃Zr dispersoids with a larger size. During hot compression testing, the addition of 0.2 wt.% Zr combined with homogenization at 450 °C increased the high-temperature flow stress by 20% relative to the base alloy free of Zr, revealing their potential to inhibit the dislocation motion and dynamic recovery. Both dispersoids were found to have positive impact on the retardation of recrystallization during post-deformation annealing, but the fine and coherent Al₃Zr dispersoids were more effective than the coarse and incoherent (Al,Si)₃Zr dispersoids.

Keywords: Zr dispersoids; Al-Mg-Si alloys, homogenization; hot deformation; recrystallization.

*Corresponding author Tel.: +1 418 550 3852.

Email address: ali.elashery1@uqac.ca.

1. Introduction

The trend to reduce vehicle fuel emissions continues to offset the effect on global warming. As a result, the industrial demand to develop light, fuel-efficient automobiles has increased rapidly. Because of their high strength-to-weight ratio, good weldability, and inherent corrosion resistance, and suitability for different product forms including extrusions, Al-Mg-Si 6xxx aluminum alloys are excellent candidates for manufacturing automotive parts, such as front rails, bumpers, and structural body components (Ref 1). During the manufacturing process of such products, 6xxx alloys undergo through hot deformation processes such as extrusion and rolling. The hot workability of a particular alloy has a direct impact on the production cost. In addition, the thermomechanical process itself can influence the material's properties including strength and ductility (Ref 2), and control of grain structure and recrystallization during hot deformation and subsequent heat treatment is of particular importance. Alloying using transition elements is an effective technique used (Ref 3–5) to achieve this goal through the formation of small and dense dispersoids which induce a pinning effect on high and low angle grain boundaries. Dispersoids can also prevent slip localization in precipitation hardened materials which is important for ductility critical applications such as crash systems. As a result, the correct distribution of such particles can inhibit recrystallization and improve mechanical properties (Ref 6,7). Dispersoids are relatively stable at high temperatures, having slow coarsening kinetics, and can therefore pin the grain boundaries and dislocations effectively during hot deformation. The desired dispersoid characteristics, e.g., size, distribution and number density, can be achieved by optimizing the homogenization treatment and the alloy chemistry (Ref 8,9).

Zirconium is widely used as a microalloying element added to Al-Zn-Mg 7xxx aluminum alloys to form fine and thermally stable dispersoids due to its low diffusion rate (Ref 5,9,10). Fine and coherent $L1_2$ - Al_3Zr dispersoids can precipitate during annealing or homogenization as a consequence of the supersaturation of Zr in the α -Al during solidification (Ref 8,11). Cubic $L1_2$ -structured Al_3Zr dispersoids form principally in the grain interior during homogenization at relatively low temperatures. It is reported that these dispersoids transform to undesirable equilibrium tetragonal DO_{23} - Al_3Zr phase during prolonged heat treatments at high temperatures (Ref 6,8,12). By using high resolution transmission electron microscopy (HRTEM), some planar faults were observed inside $L1_2$ - Al_3Zr indicative of the early stage of transformation from a cubic to tetragonal structure after high temperature treatment (Ref 13). Moreover, Himuro (Ref 14) suggested that this transformation occurred as a result of the interactions of coherent dispersoids with migrating grain boundaries during recrystallization. However, in 6xxx alloys, the presence of Si can influence the Zr dispersoid phase type by forming a different phase at high temperatures. It has been reported that Si tends to stabilize DO_{22} - $(Al,Si)_3Zr$ instead of DO_{23} - Al_3Zr through the substitution of Si for Al in the metastable Al_3Zr phase (Ref 12,13,15). In addition, Si was found to increase the nucleation rate of dispersoids by reducing the volume free energy for dispersoid formation (Ref 6).

Thermomechanical processes such as extrusion and rolling are commonly used to get the desired product form i.e., extruded profiles and sheets. Post-deformation heat treatments such as annealing or solutionizing followed by aging, are usually performed to achieve the desired mechanical properties. However, static recovery (SRV) and static recrystallization (SRX) occur during post-deformation annealing because of the high strain energy and the high density of substructures (Ref 16). For many applications the retention of a non-recrystallized structure is preferred for improving mechanical properties and corrosion resistance (Ref 9,17,18). Thermally stable Zr dispersoids have been shown to have significant impact on retarding dislocation movements and inhibiting recrystallization in aluminum alloys (Ref 9,17,19–21). Regarding 6xxx alloys, Hichem *et al.* (Ref 6) reported that the precipitation of Al_3Zr before the deformation of Al-Mg-Si alloys was effectively inhibited recrystallization. On the other hand, Meng (Ref 22) and Zou *et al.* (Ref 23) reported a reduced inhibition effect of Al_3Zr precipitates in 6xxx alloys compared to Al_3Sc and $\text{Al}_3(\text{Zr,Sc})$. Birol (Ref 24) found that the combined addition of Cr and Zr had a favorable impact on the recrystallization resistance in AA6082.

To date, there are discrepancies in the reported effects of Zr containing dispersoids on recrystallization resistance in Al-Mg-Si 6xxx alloys. Furthermore, the precipitation behavior of different types of Zr dispersoids has not been studied systematically. The present work was therefore undertaken to study the precipitation behavior of Zr dispersoids during homogenization and their effects on the recrystallization resistance in an Al-0.8%Mg-1.0%Si alloy. Different homogenization treatments were conducted at 450, 500, and 550 °C for 2 and 12 h. The microstructure evolution was characterized with optical microscopy and scanning electron microscopy. The hot deformation behavior of the alloys was evaluated by hot compression testing. The recrystallization resistance during post-deformation annealing was assessed using electron backscatter diffraction (EBSD) analysis.

2. Experimental work

Two Al-0.8%Mg-1.0%Si alloys were prepared and referred to as “base” and “0.2Zr” alloys. The chemical compositions analyzed using optical emission spectrometer are listed in Table 1. The alloys were prepared using pure Al (99.7 wt.%) and pure Mg (99.8 wt.%) as well as Al-50 wt.% Si, Al-25 wt.% Fe, and Al-15 wt.% Zr master alloys. The materials were melted using an electrical resistance furnace and cast into a permanent steel mold preheated to 250 °C to obtain rectangular ingots with dimensions of 30 mm × 40 mm × 80 mm. Different homogenization treatments were conducted on cast ingots at 450, 500 and 550 °C for 2 and 12 h with a heating rate of 100 °C/h followed by water quenching to room temperature.

Uniaxial hot compression tests were performed on a Gleeble 3800 thermomechanical simulator using cylindrical samples with a diameter of 10 mm and length of 15 mm. The compression tests involved heating the samples up to the deformation temperature (400 °C) with a heating rate of 2 °C/s and then holding for 3 minutes to ensure a uniform temperature. The samples were deformed to a true strain of 0.8 with a strain rate of 1.0 s⁻¹ followed by water quenching to retain the deformed

microstructure. Graphite foils were inserted between the cylindrical samples and the anvils to minimize the friction occurring during the deformation. To study the recrystallization resistance, a post-deformation anneal was performed at 500 °C for 4 h for selected homogenization conditions.

To reveal the microstructural features, the homogenized samples were polished using standard metallographic methods. The intermetallic phases and dispersoids were observed using optical microscopy (Nikon, Eclipse ME600) and scanning electron microscopy (SEM, JEOL-6480LV) after etching by 0.5% HF for 30 seconds. A transmission electron microscope (TEM, JEM-2100) operated at 200 kV was used to resolve the Zr dispersoids. The TEM samples were ground and electropolished using a twin-jet electropolisher operated at 15 V and -20 °C with 30 vol.% nitric acid and 70 vol.% methanol. The samples were observed in both dark and bright field modes near the [001] zone axis to reveal different types of Zr dispersoids. The average dispersoid size and number density were calculated based on a quantitative analysis of TEM images. The TEM foil thickness was measured by the convergent electron beam diffraction (CBED) method (Ref 25).

The microstructures after deformation and annealing were characterized using EBSD analysis. The EBSD samples were sectioned parallel to the deformation axis along the centerline direction, and then mounted and mechanically ground using SiC papers. The polishing was subsequently carried out using 6 μm, 3 μm diamond suspension followed by final polishing using 0.5 μm colloidal silica suspension to achieve high indexing quality. The central region of the samples was examined for the selected conditions. All-Euler orientation maps were used with a step size of 1 μm for grain structure and 0.5 μm for the quantitative measurement of the misorientation distribution of boundaries. The low angle boundaries (2-5°), medium angle boundaries (5-15°), and high angle boundaries (>15°) were presented by white, green, and black lines, respectively. To exclude the microstructure noise caused by sample preparation, misorientation angles below 2° were not considered.

3. Results and Discussion

3.1. As-cast and homogenized microstructures

Figure 1 shows backscattered SEM images of the as-cast microstructures for the base and 0.2Zr materials (Fig. 1). The microstructures of both alloys were mainly composed of α-Al with intermetallic phases distributed along interdendrite boundaries. Based on their morphologies and SEM-EDS analysis, these were identified as β-AlFeSi and primary Mg₂Si, appearing bright and dark, respectively (Fig. 1a and b). When comparing the grain structure (EBSD images, Fig. 1c and d), the base alloy exhibited a coarser grain structure with an average grain size of 211±61 μm, while the 0.2Zr alloy possessed a more uniform grain structure with an average grain size of 133±32 μm. The fine grain structure of the 0.2Zr alloy could be attributed to the primary crystals of Al₃Zr acting as nucleation sites for α-Al during solidification (Ref 26,27). The inset of Fig. 1b shows one of fine Al₃Zr primary particles formed in 0.2Zr alloy.

Figure 2 shows the optical microstructures of the base alloy for different homogenization conditions. After homogenizing at 450 °C for 2 h (Fig. 2a), a significant amount of β -Mg₂Si (indicated by arrows) was precipitated out of the matrix in areas adjacent to the β -AlFeSi and the primary Mg₂Si phases. Such areas were enriched with high supersaturation levels of Mg and Si during solidification due to the high segregation tendency of these elements towards the grain boundaries and interdendritic regions (Ref 28). Extending the homogenization time to 12 h at 450 °C promoted further precipitation of β -Mg₂Si, as shown in Fig. 2b. A reduced amount of β -Mg₂Si precipitate was observed when the temperature was increased to 500 °C compared to 450 °C for soak times up to 12 h, as shown in Figs. 2c and d. However, the primary Mg₂Si phase from the original cast structure was almost unaffected by increasing the homogenization temperature to 500 °C. Based on equilibrium calculations on the experimental compositions using ThermoCalc, a relatively high temperature of 560 °C was found to be required to dissolve the primary Mg₂Si phase in this alloy. Therefore, homogenizing at a temperature close to this temperature, namely at 550 °C, suppressed the precipitation of β -Mg₂Si precipitates and significantly dissolved the primary Mg₂Si phase into the α -Al matrix, as shown in Figs. 2e and f.

In the case of the 0.2Zr alloy (Fig. 3), a generally higher amount of β -Mg₂Si precipitate was observed compared to the base alloy (Fig. 2). This can be related to the smaller grain size and consequently the larger total grain boundary area of the 0.2Zr alloy, where the segregation of Mg and Si typically occurs. Similar to the base alloy, the precipitation of β -Mg₂Si in the 0.2Zr alloy only occurred at 450 °C and 500 °C with a reduced amount at 500 °C. The most outstanding feature of the homogenized microstructure of the 0.2Zr alloy was the presence of a large amount of Zr-bearing dispersoids which were mainly precipitated at the dendrite centre at 500 °C (Fig. 3c and d) and 550 °C (Fig. 3e and f). In addition, much smaller dispersoids precipitated at 450 °C (Fig. 4a) that could not be observed by the optical microscope. The dispersoids were distinguished from the β -Mg₂Si precipitates based on the morphology and size using SEM, where the former (black arrow) were globular and much smaller in size, and the latter (white arrow) exhibited a needle-like morphology with a larger size. It is worth noting that the amount and size of the dispersoids depended mainly on the homogenization condition as shown by SEM images in Fig. 4 and TEM images in Fig. 5.

3.2. Evolution of Zr-bearing dispersoids

The evolution of the Zr-bearing dispersoids in the 0.2Zr alloy during homogenization was studied using TEM. Figures 5a-f show bright-field TEM images for the range of homogenization conditions investigated, where precipitation of two types of Zr-bearing dispersoids was observed. Homogenization at 450 °C for 2 h (Fig. 5a) resulted in the precipitation of nano-sized spherical Zr-dispersoids with a relatively high density. These were not detected with OM and SEM observations due to their small size which ranged between 8 and 10 nm. It is well known that at relatively low temperatures, the driving force for the precipitation of Zr dispersoids is higher due to the high level

of Zr supersaturation in the matrix (Ref 27). This supersaturation leads to the precipitation of nano-sized dispersoids with a homogeneous distribution.

When the holding time at 450 °C was increased to 12h (Fig. 5b), the density of the spherical dispersoids decreased and few elongated dispersoids (black arrows) were formed. Increasing the homogenization temperature to 500 °C (Figs. 5c and d), promoted the formation of the elongated dispersoids at the expense of the spherical dispersoids; the former were found to form after only 2 h, *i.e.*, more rapidly than they did at 450 °C. When the homogenization temperature was further increased to 550 °C (Figs. 5e and f), very few spherical dispersoids were present for both holding times, while the elongated dispersoids became dominant, displaying a lower density with a coarser morphology after 12 h compared with 2 h.

To better characterize both Zr-bearing dispersoid types, the dark field TEM imaging mode was used and selected area electron diffraction patterns (SAEDPs) were recorded together with TEM-EDS analysis. The fine spherical dispersoids formed after homogenization at 450 °C for 2 h can be clearly seen in Fig. 6a. The corresponding SAEDP shown in Fig. 6b was obtained at the $[001]_{\alpha}$ zone axis and revealed faint spots from the dispersoids between the strong spots of the α -Al. The orientation relationship between the dispersoids and α -Al was observed to be $([100] \text{ Al} // [100] \text{ dispersoid})$, indicating that these dispersoids were $L1_2\text{-Al}_3\text{Zr}$ (Ref 13,29). It was reported that due to the similarity of the lattice parameters between the aluminum matrix and $L1_2\text{-Al}_3\text{Zr}$ dispersoids, these dispersoids exhibited a coherent interface with the matrix with a slight mismatch (Ref 8). The higher magnification bright field TEM image shown in Fig. 6c displays typical coarse elongated Zr-bearing dispersoids formed after homogenization at 550 °C for 12 h. These were identified as $\text{DO}_{22}\text{-(Al,Si)}_3\text{Zr}$ according to their SAEDP (Fig. 6d), which are most likely incoherent or semi-coherent to the matrix (Ref 30). This was also confirmed by TEM-EDS analysis, which revealed that they contained a considerable amount of Si besides Al and Zr, as shown in Fig. 6e. It was reported (Ref 13,14,30) that the $\text{DO}_{22}\text{-(Al,Si)}_3\text{Zr}$ phase can be transformed from the metastable $L1_2\text{-Al}_3\text{Zr}$ phase in the presence of Si, which substitutes for Al, increasing the stability of the $\text{DO}_{22}\text{-(Al,Si)}_3\text{Zr}$ phase.

The number density and the average size of each dispersoid type were quantitatively measured based on image analysis of TEM images, and results are presented in Fig. 7. The $L1_2\text{-Al}_3\text{Zr}$ dispersoids exhibited their highest number density ($4300 \text{ 1}/\mu\text{m}^3$) and smallest average size (8.5 nm) after homogenization at 450 °C for 2 h. With increasing homogenization temperature or holding time, the number density decreased, while the average size increased, reaching the minimum and maximum values ($300 \text{ 1}/\mu\text{m}^3$ and 20 nm, respectively) after homogenization at 500 °C for 12 h. Almost no $L1_2\text{-Al}_3\text{Zr}$ dispersoids were detected in the samples homogenized at 550 °C. The opposite trend was observed for the elongated $\text{DO}_{22}\text{-(Al,Si)}_3\text{Zr}$ dispersoids during homogenization. Their number density increased with higher temperature or longer time, reaching a maximum value of $155 \text{ 1}/\mu\text{m}^3$ with an average size of 96 nm when homogenized at 550 °C for 2 h. After extended time (12 h) at 550 °C, the number density of the $(\text{Al,Si})_3\text{Zr}$ dispersoids dropped to $50 \text{ 1}/\mu\text{m}^3$ while

the size increased to 178 nm, revealing a significant coarsening effect (Fig. 5f). The opposite precipitation trends of the two types of Zr-bearing dispersoids suggest the progressive transformation of the $L1_2$ - Al_3Zr dispersoids to the DO_{22} - $(Al,Si)_3Zr$ dispersoids with increasing the homogenization temperature and time.

At a relatively low temperature where the supersaturation level of Zr in the matrix is high, the diffusion rate of Zr atoms is sluggish. Therefore, the tendency for nucleation is higher than for growth which is evident by the high number density at 450 °C for 2 h. However, prolonging the soaking time allowed silicon diffusion and substitution for Al, which subsequently increased formation of DO_{22} - $(Al,Si)_3Zr$ at the expense of the metastable $L1_2$ - Al_3Zr . This also suggests that 450 °C is too high to preserve the $L1_2$ - Al_3Zr phase for an extended soaking time. The other important factor is the available amount of Si in the matrix, which is essential for the transformation process. At low temperatures, the precipitation of Mg_2Si left less silicon available in the matrix for the transformation. In contrast, high temperature homogenization dissolved both primary and β - Mg_2Si , increasing the availability of the silicon in the matrix and promoting the transformation to $(Al,Si)_3Zr$.

3.3. Hot deformation behavior

Figure 8 shows typical flow curves for both base and 0.2Zr alloys at 400 °C and a strain rate of 1 s^{-1} after different homogenized conditions. In all cases, the stress generally rose rapidly in the early stages of compression before reaching its peak value because of dislocation multiplication and the high rate of work hardening. Then, the flow stress continued to increase with increasing strain, but at a lower rate, indicating the occurrence of dynamic softening. However, work hardening was still dominant over softening due to the high deformation rate (1 s^{-1}), which leads to tangled dislocation structures (Ref 31). The peak flow stress was defined as the tangent point on the flow curve by drawing a line along the steady-state region of the flow curve, as shown in Fig. 8a.

For the base alloy (Fig. 8a), it was found that the peak flow stress increased progressively with increasing homogenization temperature, regardless of the holding time, attaining 43, 53, and 58 MPa at 450, 500, and 550 °C, respectively. Due to the absence of Zr-bearing dispersoids in the base alloy, solid solution strengthening was the major strengthening mechanism affecting the flow stress. Since the amount of equilibrium β - Mg_2Si precipitates decreased with increasing homogenization temperature (Fig. 2), which in turn enriched the α -Al solid solution with Mg and Si solutes, the solid solution strengthening was promoted, increasing the flow stress. In addition, homogenization at 550 °C dissolved the primary Mg_2Si phase in the α -Al, further increasing the solid solution strengthening and flow stress. For the 0.2Zr alloy (Fig. 8b), homogenizing at 500 or 550 °C resulted in no significant changes of the peak flow stress compared to the base alloy. However, the peak flow stress was increased by around 20 % compared to the base alloy (52 MPa vs. 46 MPa) after homogenization at 450 °C. This increase is attributed to the strengthening effect

of the large amount of coherent Al_3Zr dispersoids, which were optimally precipitated at 450 °C. The pinning effect of such dispersoids on the dislocation movement and dynamic recovery has been extensively reported in 7xxx alloys (Ref 9,19,32).

Two homogenization conditions for each alloy were selected for the investigation of the as-deformed microstructure, namely 450 °C for 2 h and 550 °C for 2h, where the spherical Al_3Zr and elongated $(\text{Al,Si})_3\text{Zr}$ dispersoids attained their highest number densities, respectively. Figure 9 shows the corresponding EBSD Euler orientation maps, which reveal different features of the as-deformed microstructures, including low angle boundaries (2° - 5°), medium angle boundaries (5° - 15°), and high angle boundaries ($>15^\circ$) represented by white, green, and black lines respectively. All maps showed elongated grains perpendicular to the compression direction along with a large number of low and medium angle boundaries, indicating the presence of high densities of dislocations and subgrains (Ref 33). It may be also noted that due to the high deformation condition (high Z), the grain boundaries exhibited serrations and bulging for all conditions. For the base alloy, no significant differences were observed between the two homogenization conditions (Fig. 9a and b). Both conditions exhibited a recovered structure with a large amount of low and medium angle grain boundaries resulting from high dislocation density generated during deformation.

EBSD mapping of the 0.2Zr alloy also revealed a recovered structure but with less homogenous deformation compared to the base alloy. This heterogenous deformation was evident by the grain subdivision (Fig. 9c) or the appearance of deformation bands (Fig. 9d). In addition, the samples homogenized at 450 °C (Fig. 9c) showed a significantly higher number density of dislocations and substructure compared to the base alloy. The high density of dislocation cells and subgrains observed at 450 °C was locally introduced due to the slow dynamic recovery with the piling-up of dislocations caused by fine Al_3Zr dispersoids (Ref 34). However, homogenization at 550 °C resulted in a more recovered structure with a reduced level of low angle boundaries (Fig. 9d), indicating less inhibition of dynamic recovery associated with the coarse $(\text{Al,Si})_3\text{Zr}$ dispersoids compared to the finer Al_3Zr dispersoids. The results are consistent with the flow curve trends in Fig. 8b, where the slope of the flow curve at 450 °C was higher than at 550 °C, corresponding to the higher inhibition of softening associated with Al_3Zr dispersoids compared to $(\text{Al,Si})_3\text{Zr}$. The increased coherency with the matrix and the smaller size of Al_3Zr dispersoids induced higher Zener-drag pinning effect on migrating subgrain boundaries during hot deformation (Ref 35,36).

3.4. Recrystallization resistance

Figure 10 shows EBSD Euler orientation maps of the microstructures of the base and 0.2Zr alloys after annealing at 500 °C for 4 h. The misorientation angle distribution and boundary fractions are presented in Fig. 11 and Table 2, respectively. The base alloy exhibited almost fully recrystallized grains after annealing regardless of the homogenization conditions, as shown in Figs. 10a and b. In contrast, the 0.2Zr alloy homogenized at 450°C/2h still retained the original elongated grains with a recovered structure (Fig. 10c), while the 550°C/2h treatment resulted in a partially recrystallized structure (Fig. 10d).

The quantitative results in Fig. 11 and Table 2 show that the annealed base alloy possessed mostly high angle grain boundaries (HAB, > 90%) after both homogenization conditions, confirming a fully recrystallized grain structure. The low recrystallization resistance of the base alloy can be attributed to the absence of particles/dispersoids with a sufficient pinning effect, which could retard the boundary migration. On the other hand, the majority of the grain boundaries in the 0.2Zr alloy after annealing were low angle boundaries (LAB). The grain structures observed in the annealed 0.2Zr alloy depended on the homogenization treatment applied. Homogenization at 450 °C for 2 h, resulted in a recovered structure with a high density of low angle boundaries, as shown in Figs. 10c and 11c. Only a very small number of recrystallized grains was observed near original grain boundaries (arrowed in Fig. 10c). The misorientation angle distribution in Fig. 11c showed a high fraction (82.3 %) of low angle boundaries (LAB) with a mean angle of 10.6°, indicating a strong inhibiting effect of fine spherical dispersoids Al₃Zr on the dislocation polygonization and subgrain coalescence. After homogenization at 550 °C for 2 h (Fig. 10d and 11d), the density of LAB was substantially reduced, and correspondingly HAB were increased. An increased number of coarse grains featuring no internal substructure were also observed along grain boundaries (arrowed in Fig. 10d), indicating a higher growth rate of recrystallized grains during annealing as compared to after homogenization at 450 °C for 2 h. The misorientation angle distribution (Fig. 11d and Table 2) also reflected a clear increase in the fractions of HAB for the higher temperature treatment (38.3 % at 550 °C for 2 h vs. 17.7% at 450 °C for 2 h) and increase in mean misorientation angle (17.9° at 550 °C for 2 h vs. 10.6° at 450 °C for 2 h) relative to homogenization at 450 °C for 2 h. These results indicate that the elongated (Al,Si)₃Zr were less effective at inhibiting recrystallization than the fine Al₃Zr dispersoids.

According to the expression for Zener pinning (Ref 9,37), particles having a smaller size and higher volume fraction produce a higher pinning force. Moreover, there are two other essential particle features controlling the grain boundary pinning effect, namely the interface coherency and the uniformity of the particle distribution within the microstructure. Regarding the coherency, the maximum pinning force associated with coherent dispersoids was reported by Liu (Ref 17) to be twice that produced by incoherent dispersoids of the same size. Therefore, the smaller, coherent Al₃Zr dispersoids in the present study were more effective at inhibiting boundary migration and consequently in increasing the recrystallization resistance compared to the coarse, incoherent (Al,Si)₃Zr dispersoids. The other important factor is the dispersoid free zones (DFZs) arising from the non-homogeneous distribution of Zr in the matrix during solidification, which leads to an uneven distribution of dispersoids (Ref 9,19,35). During high temperature homogenization, more Si becomes available due to the dissolution of primary Mg₂Si into the matrix, promoting (Al,Si)₃Zr dispersoid formation in the dendrite centers. Figure 12a shows the distribution of (Al,Si)₃Zr dispersoids after homogenization at 550 °C for 2 h using a dark field optical micrograph. There was a high number density of dispersoids in the dendrite centers, but large DFZs were observed at interdendritic and grain boundaries up to 10 μm in width. Therefore, recrystallization during annealing was more likely to occur in DFZs along the grain boundaries. The DFZs associated with Al₃Zr dispersoids formed during low-temperature homogenization at 450 °C were significantly

narrower (~450 nm, Fig. 12b), and this further contributed to the effectiveness of the Al_3Zr dispersoids at inhibition of recrystallization.

4. Conclusions

The evolution of Zr-bearing dispersoids in an Al-0.8%Mg-1.0%Si alloy and their effect on hot deformation and recrystallisation resistance were studied under different homogenization conditions. The following conclusions can be drawn:

1. Two types of Zr-bearing dispersoids can be precipitated in Al-0.8%Mg-1.0%Si alloy with an addition of 0.2 wt.% Zr, depending on the homogenization conditions. Homogenization at 450 °C for 2 h resulted in the precipitation of fine and coherent $\text{L1}_2\text{-Al}_3\text{Zr}$ dispersoids. With increasing homogenization temperature and/or time, elongated and incoherent $\text{DO}_{22}\text{-(Al,Si)}_3\text{Zr}$ dispersoids were formed, which dominated the microstructure when homogenized at 550 °C.
2. The addition of 0.2 wt.% Zr combined with homogenization at 450 °C produced a high density of fine Al_3Zr dispersoids (~10 nm) with a uniform distribution, increasing the high-temperature flow stress by 20% relative to the base alloy free of Zr, and promoting a strong Zener pinning effect on dislocation movement and a high inhibiting effect on dynamic recovery.
3. The addition of 0.2 wt.% Zr combined with homogenization at a conventional temperature of 550 °C produced a low density of coarser $\text{(AlSi)}_3\text{Zr}$ dispersoids (100-200 nm), which had a minimal effect on high-temperature flow stress and a moderate effect on the retardation of dynamic recovery.
4. Both dispersoid types were found to increase the recrystallization resistance during post-deformation annealing. However, the pinning effect of the Al_3Zr dispersoids and hence the corresponded recrystallization resistance was significantly higher than that of the $\text{(Al,Si)}_3\text{Zr}$ dispersoids. As a result, selection of the homogenisation treatment is critical to control the Zr dispersoid type and the microstructure evolution during thermomechanical treatment.

Acknowledgments

The authors would like to acknowledge the financial support of the Natural Sciences and Engineering Research Council of Canada (NSERC) under the Grant No. CRDPJ 514651-17 and Rio Tinto Aluminum through the Research Chair in the Metallurgy of Aluminum Transformation at University of Quebec at Chicoutimi.

References

1. J. HIRSCH, Recent Development in Aluminium for Automotive Applications, *Trans. Nonferrous Met. Soc. China*, 2014, **24**(7), p 1995–2002.
2. J. Ren, Z. Chen, J. Peng, W. Ma, and S.P. Ringer, An Initial Report on Achieving High Comprehensive Performance in an Al-Mg-Si Alloy via Novel Thermomechanical Processing, *J. Alloys Compd.*, 2018, **764**, p 679–683.
3. R. Guemini, A. Boubertakh, and G.W. Lorimer, Study of the Recrystallization Process of AlMgSi Alloys Containing Transition Elements, *J. Alloys Compd.*, 2009, **486**(1–2), p 451–457.
4. Q. Dong, A. Howells, M.F. Gallerneault, and V. Fallah, Precipitation-Induced Mitigation of Recrystallization in Ultra-Thin, Cold-Rolled AlScZrMn(Mg) Sheets at Brazing Temperatures: The Critical Effect of Alloy Composition and Thermal Processing Route, *Acta Mater.*, 2020, **186**, p 308–323.
5. V. V. Zakharov, About Alloying of Aluminum Alloys with Transition Metals, *Met. Sci. Heat Treat.*, Springer New York LLC, 2017, **59**(1–2), p 67–71.
6. F. Hichem and G. Rebai, Study of Dispersoid Particles in Two Al–Mg–Si Aluminium Alloys and Their Effects on the Recrystallization, *Appl. Phys. A*, Springer Verlag, 2015, **119**(1), p 285–289.
7. F. Kahrıman and M. Zeren, The Effect of Zr on Aging Kinetics and Properties of As-Cast AA6082 Alloy, *Int. J. Met.*, Springer, 2017, **11**(2), p 216–222.
8. A.V. Mikhaylovskaya, A.G. Mochugovskiy, V.S. Levchenko, N.Y. Tabachkova, W. Mufalo, and V.K. Portnoy, Precipitation Behavior of L12 Al₃Zr Phase in Al-Mg-Zr Alloy, *Mater. Charact.*, Elsevier Inc., 2018, **139**, p 30–37.
9. Z. Guo, G. Zhao, and X.-G. Chen, Effects of Two-Step Homogenization on Precipitation Behavior of Al₃Zr Dispersoids and Recrystallization Resistance in 7150 Aluminum Alloy, *Mater. Charact.*, Elsevier Inc., 2015, **102**, p 122–130.
10. A.M. Cassell, J.D. Robson, C.P. Race, A. Eggeman, T. Hashimoto, and M. Besel, Dispersoid Composition in Zirconium Containing Al-Zn-Mg-Cu (AA7010) Aluminium Alloy, *Acta Mater.*, 2019, **169**, p 135–146.
11. C. Shi and X.-G. Chen, Effects of Zr and v Micro-Alloying on Activation Energy During Hot Deformation of 7150 Aluminum Alloys, *Light Metals 2015*, (Hoboken, NJ, USA), John Wiley & Sons, Inc., 2015, p 163–167.
12. F. Kahrıman and M. Zeren, Microstructural and Mechanical Characterization of Al-0.80Mg-0.85Si-0.3Zr Alloy, *Arch. Foundry Eng.*, De Gruyter Open Ltd, 2017, **17**(4), p 73–78.
13. L. LITYŃSKA, D. ABOU-RAS, G. KOSTORZ, and J. DUTKIEWICZ, TEM and HREM Study of Al₃Zr Precipitates in an Al-Mg-Si-Zr Alloy, *J. Microsc.*, 2006, **223**(3), p 182–184.

14. Y. Himuro, K. Koyama, and Y. Bekki, Precipitation Behaviour of Zirconium Compounds in Zr-Bearing Al-Mg-Si Alloy, *Mater. Sci. Forum*, Trans Tech Publ, 2006, **519–521**(PART 1), p 501–506.
15. F. Kahrıman and M. Zeren, Mechanical and Fractographical Characterization of Extruded Al-Mg-Si-Zr Alloys, *MATEC Web Conf.*, S. Pantelakis and S. Koubias, Eds., 2018, **188**, p 02017.
16. C. Poletti, M. Rodriguez-Hortalá, M. Hauser, and C. Sommitsch, Microstructure Development in Hot Deformed AA6082, *Mater. Sci. Eng. A*, 2011, **528**(6), p 2423–2430.
17. S. Liu, J. Chen, W. Chai, Q. Wang, Z. Yang, L. Ye, and J. Tang, Effects of Combined Additions of Mn and Zr on Dispersoid Formation and Recrystallization Behavior in Al-Zn-Mg Alloys, *Metall. Mater. Trans. A*, Springer Boston, 2019, **50**(10), p 4877–4890.
18. A.R. Eivani, H. Ahmed, J. Zhou, and J. Duszczyk, An Experimental and Theoretical Investigation of the Formation of Zr-Containing Dispersoids in Al-4.5Zn-1Mg Aluminum Alloy, *Mater. Sci. Eng. A*, 2010, **527**(9), p 2418–2430.
19. B. Morere, R. Shahani, C. Maurice, and J. Driver, The Influence of Al₃Zr Dispersoids on the Recrystallization of Hot-Deformed AA 7010 Alloys, *Metall. Mater. Trans. A*, 2001, **32**(3), p 625–632.
20. C. Shi and X.-G. Chen, Effect of Zr Addition on Hot Deformation Behavior and Microstructural Evolution of AA7150 Aluminum Alloy, *Mater. Sci. Eng. A*, 2014, **596**, p 183–193.
21. H. Li, Z. Gao, H. Yin, H. Jiang, X. Su, and J. Bin, Effects of Er and Zr Additions on Precipitation and Recrystallization of Pure Aluminum, *Scr. Mater.*, 2013, **68**(1), p 59–62.
22. Y. MENG, Z. ZHAO, and J. CUI, Effect of Minor Zr and Sc on Microstructures and Mechanical Properties of Al-Mg-Si-Cu-Cr-V Alloys, *Trans. Nonferrous Met. Soc. China*, 2013, **23**(7), p 1882–1889.
23. L. Zou, Q.-L. Pan, Y.-B. He, W.-J. Liang, and C.-Z. Wang, Microstructures and Tensile Properties of Al-Zn-Cu-Mg-Zr Alloys Modified with Scandium, *Mater. Sci.*, Springer, 2008, **44**(1), p 120.
24. Y. Birol, Effect of Cr and Zr on the Grain Structure of Extruded EN AW 6082 Alloy, *Met. Mater. Int.*, 2014, **20**(4), p 727–732.
25. J.M. Cowley, Electron Microdiffraction, *Advances in Electronics and Electron Physics*, Springer Science & Business Media, 1978, p 1–53.
26. F. Wang, D. Qiu, Z.-L. Liu, J.A. Taylor, M.A. Easton, and M.-X. Zhang, The Grain Refinement Mechanism of Cast Aluminium by Zirconium, *Acta Mater.*, 2013, **61**(15), p 5636–5645.
27. E. Clouet, J.M. Sanchez, and C. Sigli, First-Principles Study of the Solubility of Zr in Al, *Phys. Rev. B*, APS, 2002, **65**(9), p 094105.
28. S.N. Samaras and G.N. Haidemenopoulos, Modelling of Microsegregation and Homogenization of 6061 Extrudable Al-Alloy, *J. Mater. Process. Technol.*, 2007, **194**(1–

- 3), p 63–73.
29. H. Farh, K. Djemmal, R. Guemini, and F. Serradj, Nucleation of Dispersoids Study in Some Al-Mg-Si Alloys, *Ann. Chim. Sci. des Matériaux*, ELSEVIER FRANCE-EDITIONS SCIENTIFIQUES MEDICALES ELSEVIER 23 RUE LINOIS ..., 2010, **35**(5), p 283–289.
 30. T. Sato, A. Kamio, and G.W. Lorimer, Effects of Si and Ti Additions on the Nucleation and Phase Stability of the L1₂-Type Al₃Zr Phase in Al-Zr Alloys, *Mater. Sci. Forum*, 1996, **217–222**(PART 2), p 895–900.
 31. M.R. Rokni, A. Zarei-Hanzaki, A.A. Roostaei, and H.R. Abedi, An Investigation into the Hot Deformation Characteristics of 7075 Aluminum Alloy, *Mater. Des.*, 2011, **32**(4), p 2339–2344.
 32. D. LI, D. ZHANG, S. LIU, Z. SHAN, X. ZHANG, Q. WANG, and S. HAN, Dynamic Recrystallization Behavior of 7085 Aluminum Alloy during Hot Deformation, *Trans. Nonferrous Met. Soc. China*, 2016, **26**(6), p 1491–1497.
 33. M. Shakiba, N. Parson, and X.-G. Chen, Hot Deformation Behavior and Rate-Controlling Mechanism in Dilute Al-Fe-Si Alloys with Minor Additions of Mn and Cu, *Mater. Sci. Eng. A*, 2015, **636**, p 572–581.
 34. C. Shi and X.-G. Chen, Effect of Vanadium on Hot Deformation and Microstructural Evolution of 7150 Aluminum Alloy, *Mater. Sci. Eng. A*, 2014, **613**, p 91–102.
 35. Z. Jia, G. Hu, B. Forbord, and J.K. Solberg, Effect of Homogenization and Alloying Elements on Recrystallization Resistance of Al-Zr-Mn Alloys, *Mater. Sci. Eng. A*, 2007, **444**(1–2), p 284–290.
 36. Wu, Y., Liu, C., Liao, H., Jiang, J. and Ma, A, Joint effect of micro-sized Si particles and nano-sized dispersoids on the flow behavior and dynamic recrystallization of near-eutectic Al-Si based alloys during hot compression. *J. Alloys Compd.*, 2021, **856**, p.158072.
 37. J. Lai, C. Shi, and X.-G. Chen, Effects of V Addition on Recrystallization Resistance of 7150 Aluminum Alloy after Simulative Hot Deformation, *Mater. Charact.*, 2014, **96**, p 126–134.

Figure Captions

Fig. 1. SEM images of as-cast microstructure and EBSD images of grain distribution for the base (a,c) and 0.2Zr (b,d) alloys.

Fig. 2. Optical micrographs showing the microstructures of base alloy for different homogenization conditions.

Fig. 3. Optical micrographs showing the microstructures of 0.2Zr alloy for different homogenization conditions. The arrows in (d) and (e) indicate dispersoid zones (DZs).

Fig. 4. SEM images showing the Zr bearing dispersoids of 0.2Zr alloy after homogenization at 450 °C (a), 500 °C (b), and 550 °C (c) for 12 h soaking time.

Fig. 5. Bright field TEM images of 0.2Zr alloy for different homogenization conditions: (a,b) 450 °C for 2 and 12 h, (c,d) 500 °C for 2 and 12 h, and (e,f) 550 °C for 2 and 12 h.

Fig. 6. Identification of Zr-bearing dispersoids: (a) dark field TEM image showing $L1_2\text{-Al}_3\text{Zr}$ dispersoids after homogenization at 450 °C for 2 h; (b) SAEDP corresponding to (a); (c) bright field TEM image showing $\text{DO}_{22}\text{-(Al,Si)}_3\text{Zr}$ dispersoids after homogenization at 550 °C for 12 h; (d) SAEDP corresponding to (c); and (e) TEM-EDS analysis of $\text{DO}_{22}\text{-(Al,Si)}_3\text{Zr}$ dispersoids.

Fig. 7. Number density (a) and average size (b) of $L1_2\text{-Al}_3\text{Zr}$ and $\text{DO}_{22}\text{-(Al,Si)}_3\text{Zr}$ dispersoids at different homogenization conditions.

Fig. 8. Typical flow curves at 400°C and 1 s^{-1} strain rate: (a) base alloy and (b) 0.2Zr alloy. WH stands for the work hardening which mainly controls the flow behavior in the first stages of compression, while WH + DS stands for both the work hardening and the dynamic softening after reaching the peak flow stress.

Fig. 9. Euler orientation maps of as-deformed structures after hot deformation ($400 \text{ °C}, 1 \text{ s}^{-1}$) of the base alloy (a, b) and 0.2Zr alloy (c, d) homogenized at $450\text{°C}/2\text{h}$ and $550\text{°C}/2\text{hr}$, respectively. Low angle ($2^\circ\text{-}5^\circ$), medium angle ($5^\circ\text{-}15^\circ$), and high angle boundaries ($>15^\circ$) were represented by white, green, and black lines, respectively.

Fig. 10. Euler orientation maps after annealing (500 °C for 4 h) for the base (a, b) and 0.2Zr alloys (c, d) for two homogenization conditions ($450\text{°C}/2\text{h}$ and $550\text{°C}/2\text{h}$). Low angle ($2^\circ\text{-}5^\circ$), medium angle ($5^\circ\text{-}15^\circ$), and high angle boundaries ($>15^\circ$) are represented by white, green, and black lines, respectively.

Fig. 11. Misorientation angle distribution for base and 0.2Zr alloys for different homogenization conditions after annealing treatment at 500 °C for 4 h.

Fig. 12. OM dark field image (a) and dark field TEM image (b) of 0.2Zr alloy homogenized at 550°C/2h (a) and 450°C/2h (b), respectively.

Tables

Table 1. Chemical composition (wt.%) of the experimental alloys.

Alloy	Mg	Si	Fe	Zr	Ti	Al
Base	0.81	1.05	0.18	---	0.15	Bal.
0.2Zr	0.83	1.01	0.20	0.193	0.11	Bal.

Table 2. Quantitative analysis of EBSD results.

Alloy	Homogenization condition	LAB (<15°) fraction, %	HAB (≥15°) fraction, %	Mean angle boundary, °
Base	450°C/2h	9.4	90.6	34.6
	550°C/2h	6.3	93.7	36.2
0.2Zr	450°C/2h	82.3	17.7	10.6
	550°C/2h	61.7	38.3	17.9

Figures

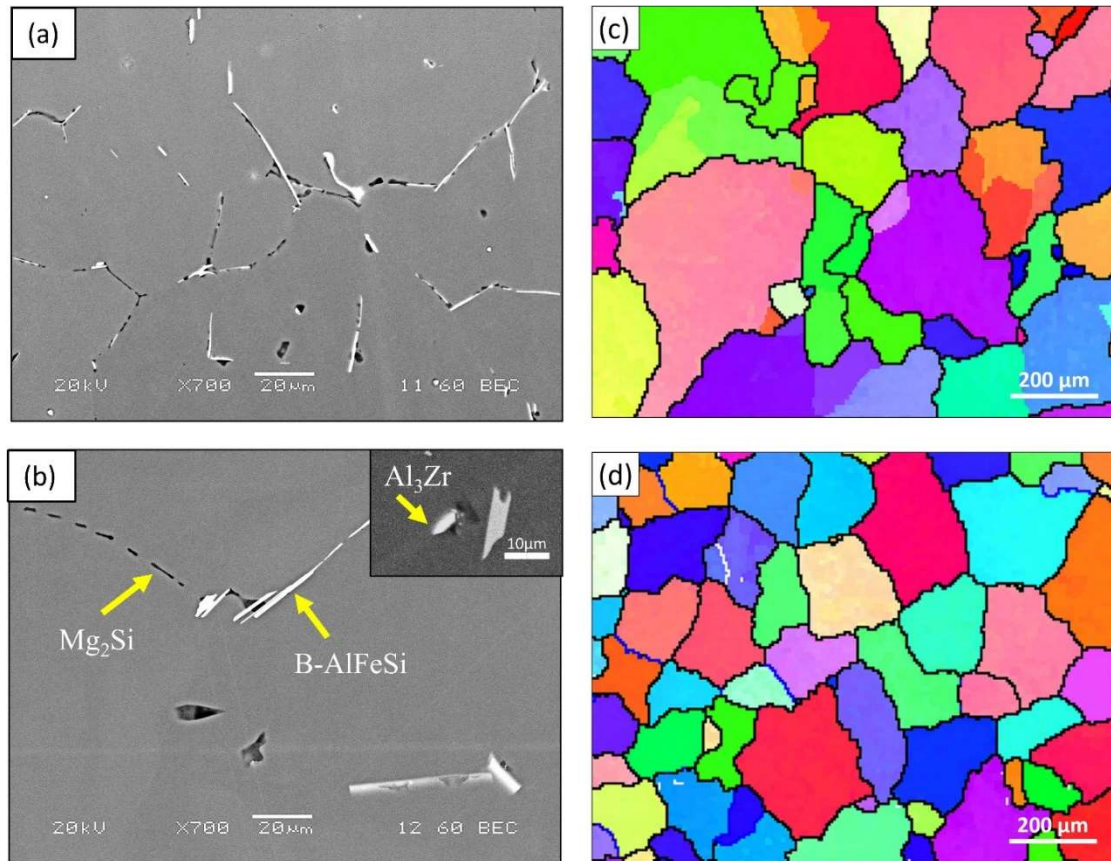


Fig. 1. SEM images of as-cast microstructure and EBSD images of grain distribution for the base (a,c) and 0.2Zr (b,d) alloys.

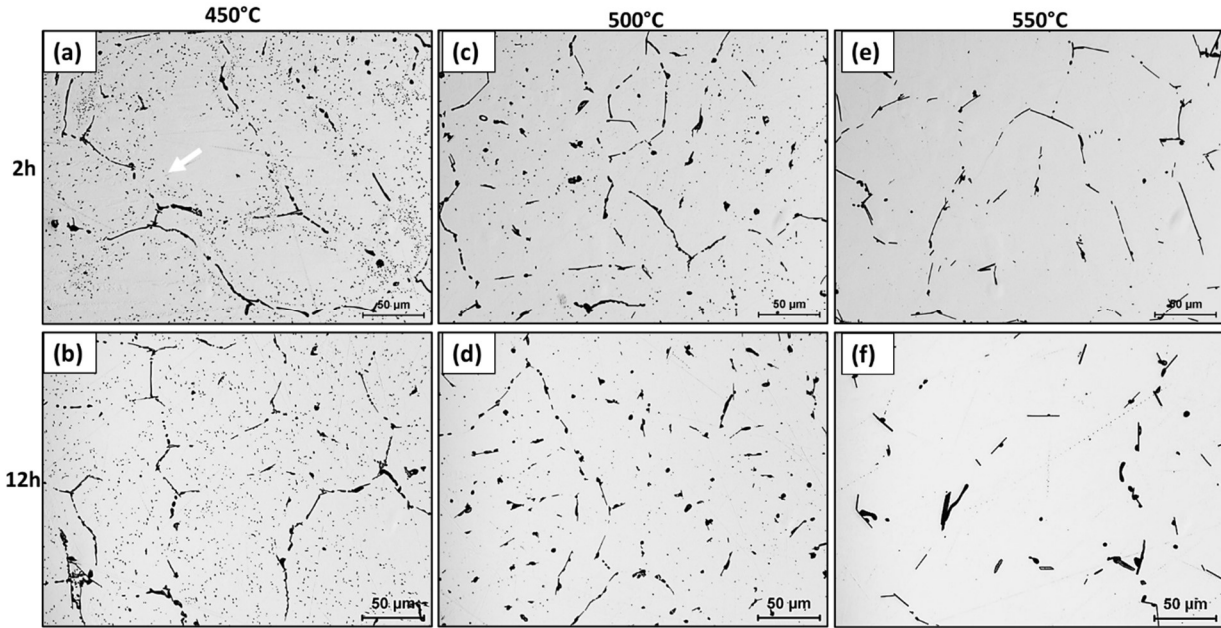


Fig. 2. Optical micrographs showing the microstructures of base alloy for different homogenization conditions.

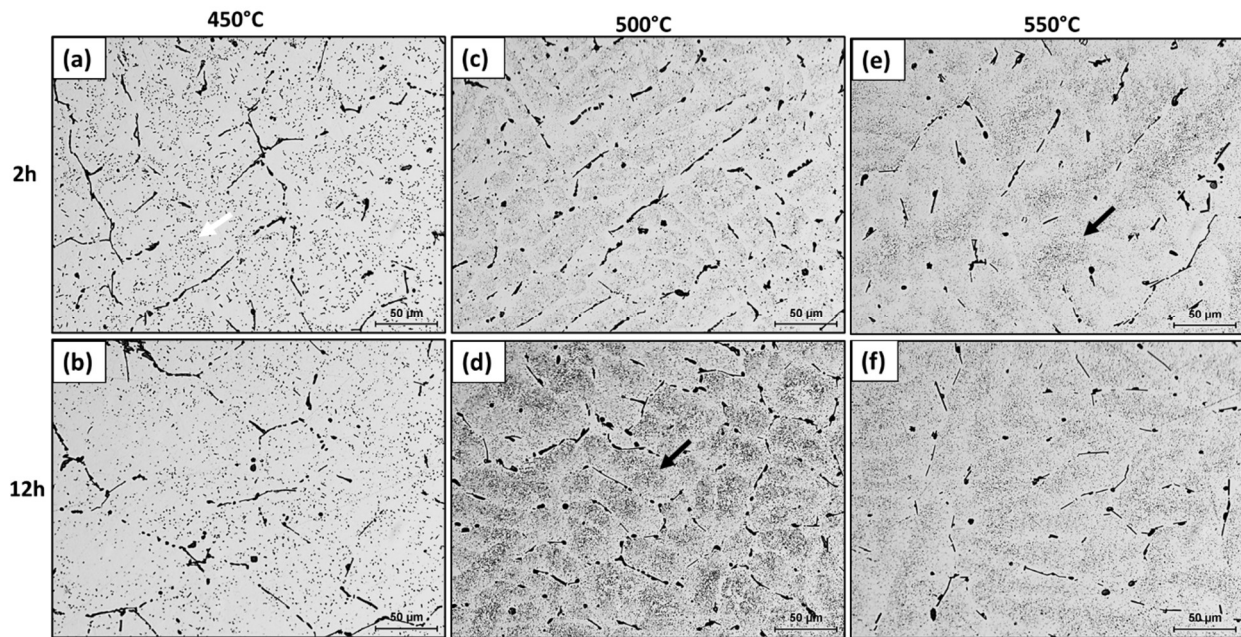


Fig. 3. Optical micrographs showing the microstructures of 0.2Zr alloy for different homogenization conditions. The arrows in (d) and (e) indicate dispersoid zones (DZs).

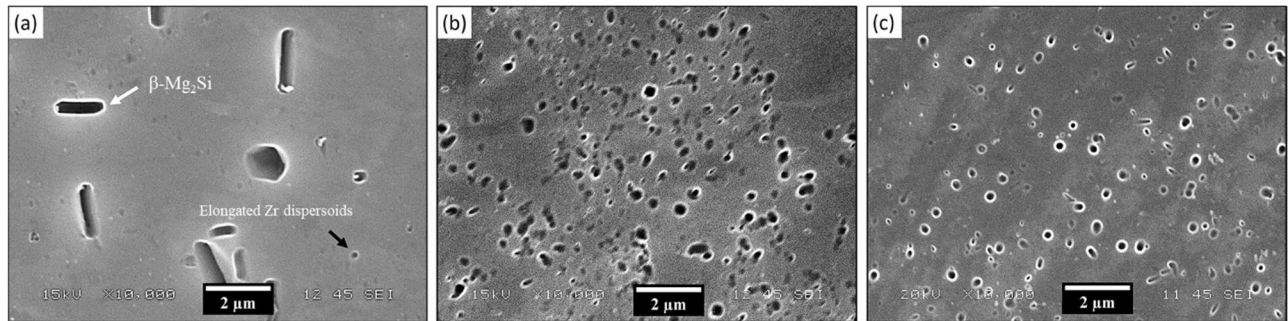


Fig. 4. SEM images showing the Zr bearing dispersoids of 0.2Zr alloy after homogenization at 450 °C (a), 500 °C (b), and 550 °C (c) for 12 h soaking time.

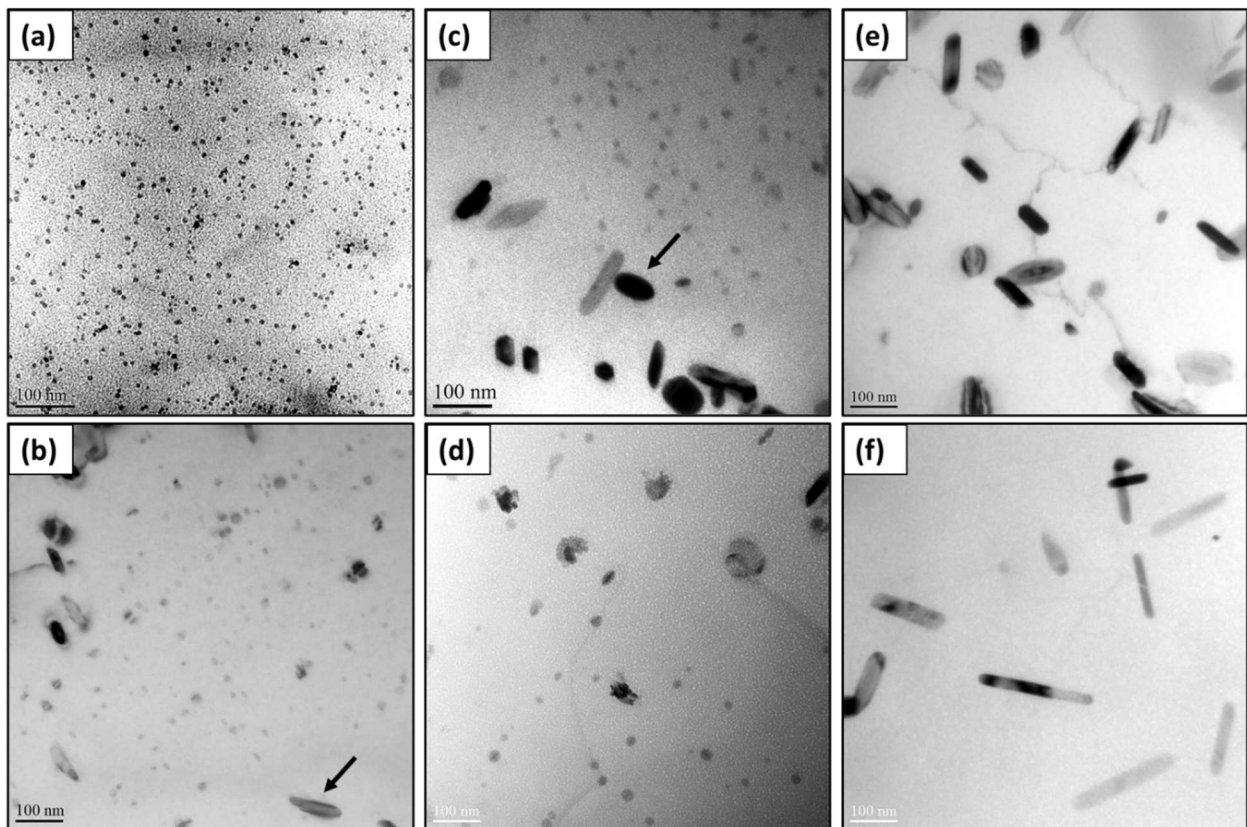


Fig. 5. Bright field TEM images of 0.2Zr alloy for different homogenization conditions: (a,b) 450 °C for 2 and 12 h, (c,d) 500 °C for 2 and 12 h, and (e,f) 550 °C for 2 and 12 h.

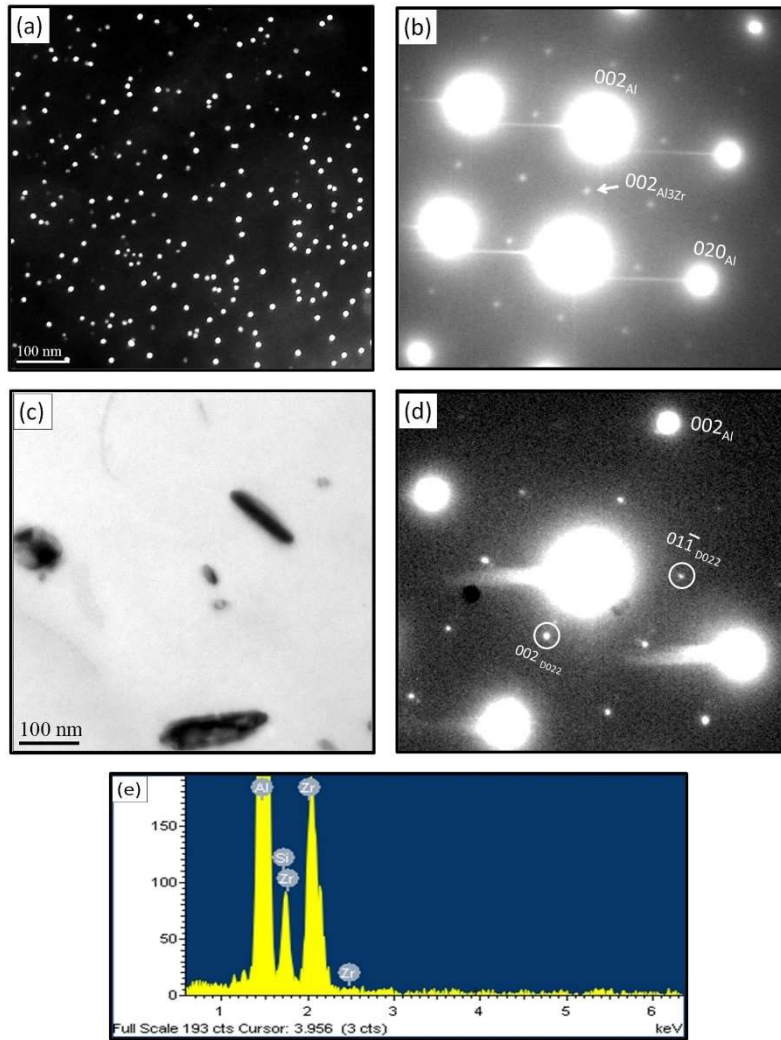


Fig. 6. Identification of Zr-bearing dispersoids: (a) dark field TEM image showing $L1_2$ - Al_3Zr dispersoids after homogenization at 450 °C for 2 h; (b) SAEDP corresponding to (a); (c) bright field TEM image showing DO_{22} - $(Al,Si)_3Zr$ dispersoids after homogenization at 550 °C for 12 h; (d) SAEDP corresponding to (c); and (e) TEM-EDS analysis of DO_{22} - $(Al,Si)_3Zr$ dispersoids.

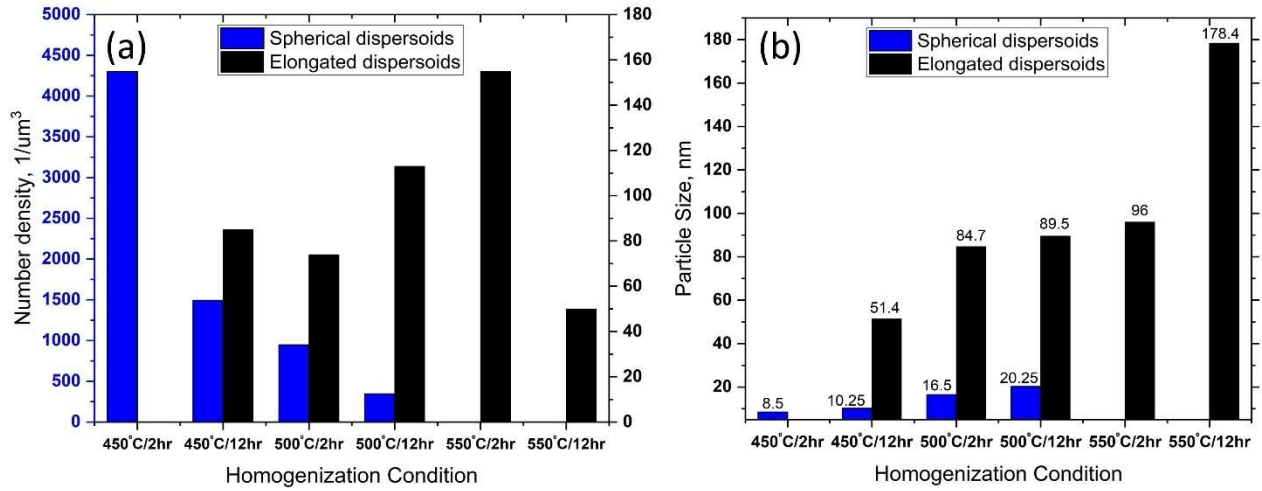


Fig. 7. Number density (a) and average size (b) of L_{12} - Al_3Zr and DO_{22} - $(Al,Si)_3Zr$ dispersoids at different homogenization conditions.

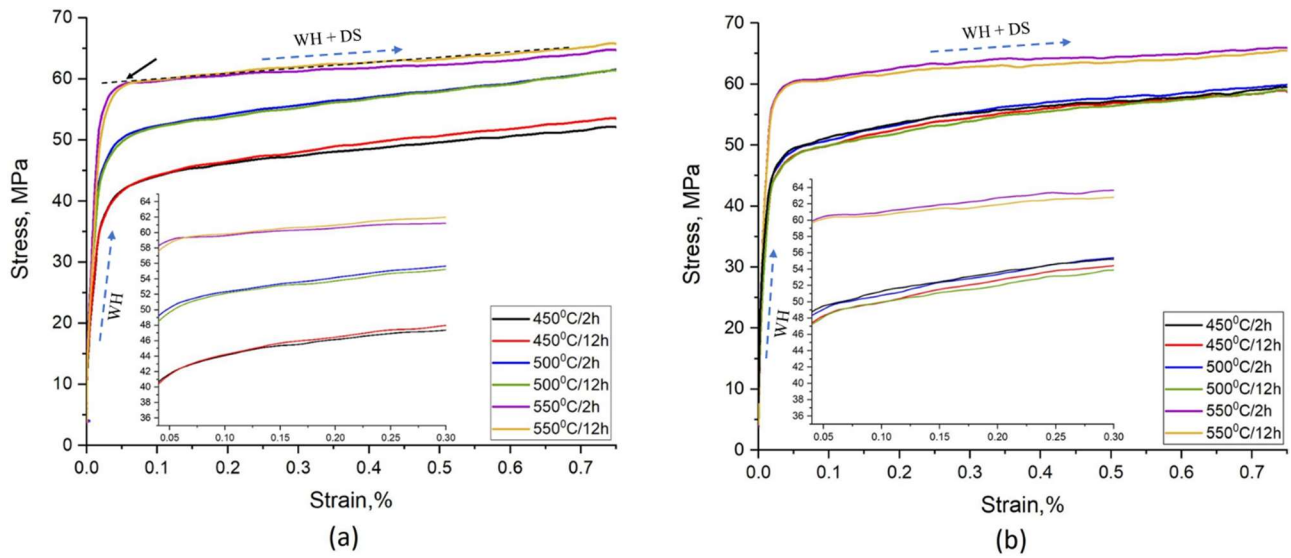


Fig. 8. Typical flow curves at 400 °C and 1 s⁻¹ strain rate: (a) base alloy and (b) 0.2Zr alloy. WH stands for the work hardening which mainly controls the flow behavior in the first stages of compression, while WH + DS stands for both the work hardening and the dynamic softening after reaching the peak flow stress. (Note: In Fig. 8a and b, the label in the x-axis is “Strain” instead of “Strain, %”, which is corrected in the final version)

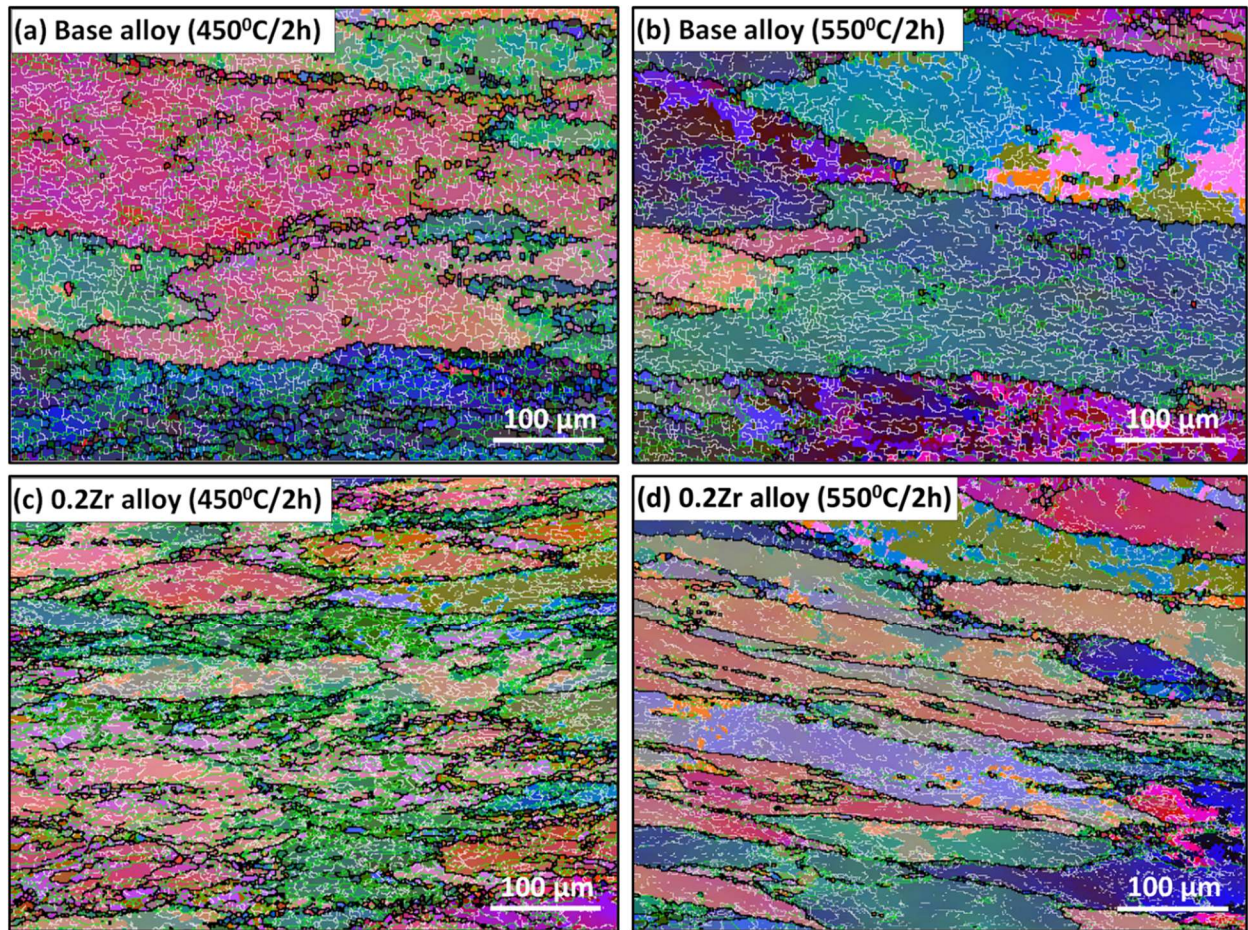


Fig. 9. Euler orientation maps of as-deformed structures after hot deformation ($400\text{ }^{\circ}\text{C}, 1\text{ s}^{-1}$) of the base alloy (a, b) and 0.2Zr alloy (c, d) homogenized at $450^{\circ}\text{C}/2\text{h}$ and $550^{\circ}\text{C}/2\text{hr}$, respectively. Low angle (2° - 5°), medium angle (5° - 15°), and high angle boundaries ($>15^{\circ}$) are represented by white, green, and black lines, respectively.

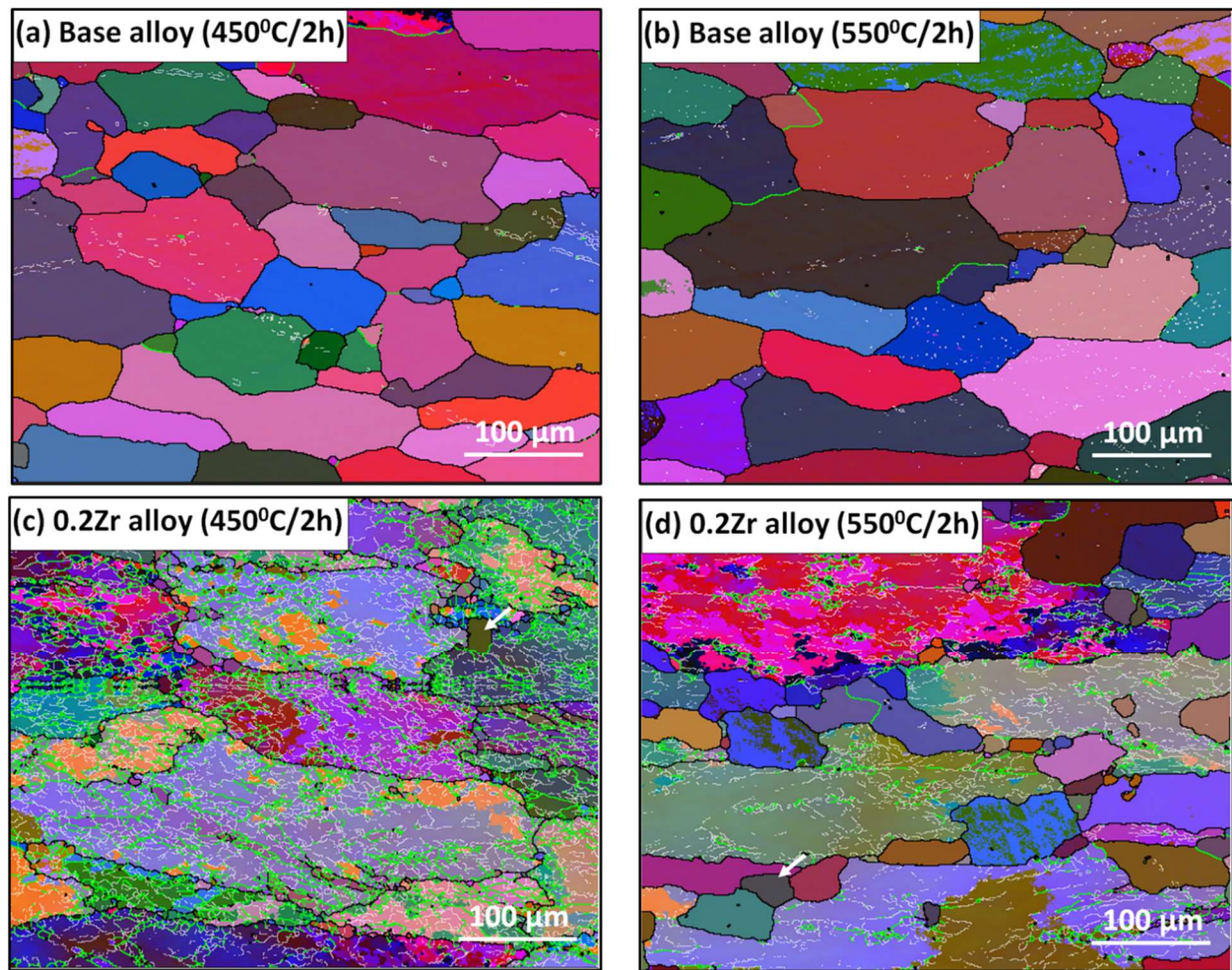


Fig. 10. Euler orientation maps after annealing (500 °C for 4 h) for the base (a, b) and 0.2Zr alloys (c, d) for two homogenization conditions (450°C/2h and 550°C/2h). Low angle (2°-5°), medium angle (5°-15°), and high angle boundaries (>15°) are represented by white, green, and black lines, respectively.

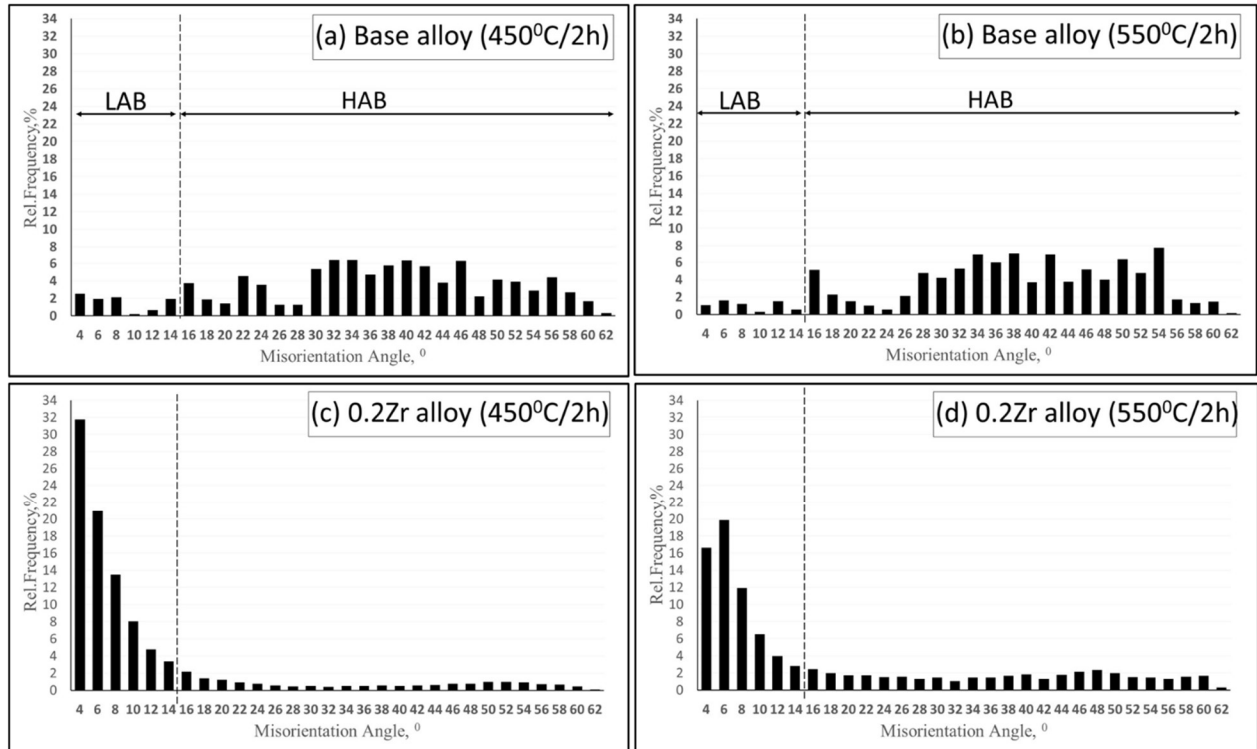


Fig. 11. Misorientation angle distribution for base and 0.2Zr alloys for different homogenization conditions after annealing treatment at 500 °C for 4 h.

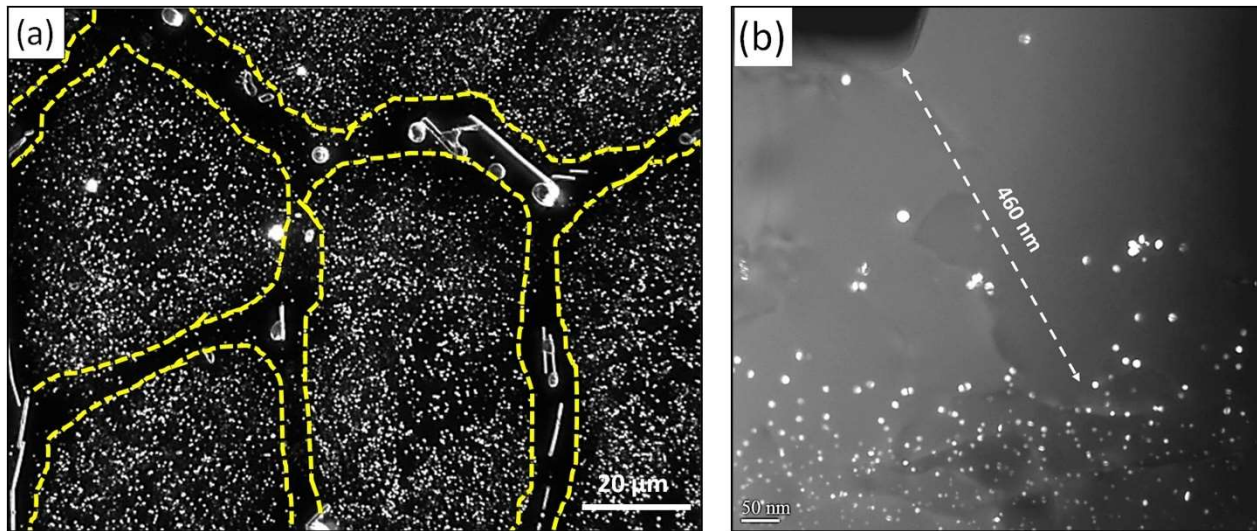


Fig. 12. OM dark field image (a) and dark field TEM image (b) of 0.2Zr alloy homogenized at 550°C/2h (a) and 450°C/2h (b), respectively.